Powell Lens-based Spectral Domain Line-Field Optical Coherence Tomography system for cellular resolution imaging of biological tissue

KEYU CHEN,[1] WEIXIANG SONG,[1] LE HAN,[1] AND KOSTADINKA BIZHEVA[1,2,3,*]

[1]*Department of Physics and Astronomy, University of Waterloo, Waterloo, Ontario N2L 3G1, Canada*
[2]*School of Optometry and Vision Sciences, University of Waterloo, Waterloo, Ontario, Canada*
[3]*System Design Engineering Department, University of Waterloo, Waterloo, Ontario N2L 3G1, Canada*
**kbizheva@uwaterloo.ca*

Abstract: A Powell lens is used in a Line-Field Spectral Domain OCT (PL-LF-SD-OCT) system to generate a line-shaped imaging beam with almost uniform distribution of the optical power in the line direction. This design overcomes the severe sensitivity loss (~10 dB) observed along the line length (B-scan width) in LF-OCT systems based on cylindrical lens line generators. The PL-LF-SD-OCT system offers almost isotropic spatial resolution (Δx and Δy ~2 μm, Δz ~1.8 μm) in free space and sensitivity of ~87 dB for 2.5 mW imaging power and 2,000 fps imaging rate, with only ~1.6 dB sensitivity loss along the line length. Images acquired with the PL-LF-SD-OCT system allow for visualization of the cellular and sub-cellular structure of biological tissues.

1. Introduction

OCT technology can be classified in 3 categories based on the scanning approach used for generation of volumetric images[1]. In point-scanning OCT (PS-OCT) a focused Gaussian beam is raster scanned in the transverse (XY) plane simultaneously with recording depth for generation of a 3D image. Jitter from the mechanical scanning causes phase instability in the X and Y directions in the acquired imaging data. This phase instability can hinder the ability of OCT technology to measure accurately blood flow or functional responses of neural tissue to external stimulation. In Full Field OCT (FF-OCT), a wide optical beam is incident on the surface of the imaged object and scattered light from is projected onto the sensor of a 2D camera. Volumetric FF-OCT images are acquired by translating the focal plane in Z direction. Since there is no mechanical scanning in the XY plane, FF-OCT offers high phase stability in the transverse imaging plane[1,2]. In Line-Scan (LS) or Line-Field (LF) OCT, a line shaped beam is projected onto the surface of the imaged object and scanned in Y direction while data in Z direction is acquired simultaneously to form a volumetric image[3]. Therefore, LS-OCT offers high phase stability in the XZ plane with some scanning mirror jitter related phase instability in the Y scanning direction[4].

While the concept of LS-OCT was first proposed nearly two decades ago [5], it took more than a decade for suitable fast, 2D camera technology to be developed. Over the past ~10 years multiple research groups have developed LS-OCT for structural[6], vascular[7,8] and functional[9-11] imaging of the human retina, cellular resolution imaging of the human cornea and limbus [12], as well as cellular resolution imaging of human skin[13-16].

Almost all LS-OCT systems that have been reported so far use a cylindrical lens as the line generator, which results in an elliptically shaped transverse profile of the beam with Gaussian intensity distribution along the major and minor axis of the ellipse. This leads to progressive loss of image contrast from the center of the line (B-scan width) to its edges. The typical quick solution to this problem adopted by many research groups is to simply cut the low contrast areas of the acquired LS-OCT image. However, this approach is wasteful as it reduces

significantly the image FOV. An alternative approach is to replace the cylindrical lens with a Powell lens, which generates a top-hat light intensity profile in the line-direction. The Powell lens has been used as line generator for numerous industrial applications for decades since its invention[17]. However, the first Powell lens-based LS-SD-OCT (PL-LS-SD-OCT) system was only reported recently[18]. While the design of this system is compact, simple and likely offers easy optical alignment, it has significant limitations in terms of spatial resolution and sensitivity. The authors used 15 mW optical power incident on the imaged biological tissue sample to achieve ~87 dB maximum sensitivity at an imaging rate of 3,500. This power exceeds the maximum permissible exposure (MPE) for ocular tissues as defined by the ANSI standard [19] by more than 3×. Furthermore, the system has ~16 dB sensitivity roll-off and nearly 2× degradation of the FWHM of the axial PSF over a scanning range of ~ 850 µm. Therefore, this design of the PL-LS-SD-OCT system may not be suitable for ophthalmic applications.

Here, a novel design of a PL-LS-SD-OCT system is presented, which offers ~2 µm × 2 µm × 1.8 µm (x × y × z) resolution in free space, ~87 dB maximum for 2.5 mW imaging power at 2,000 fps image acquisition rate. More importantly, the sensitivity loss in a single B-scan along the line direction is only ~1.6 dB. The system was validated by imaging plant tissue (cucumber) and animal cornea (rats).

2. Methods

2.1 Powell lens

Line generators such as cylindrical lenses and Powell lenses are designed to convert circularly-shaped optical beams to line-shaped beams by restricting the propagation of light in one of the transverse directions of the beam (X or Y). Cylindrical lenses utilize a spherically-shaped front surface to convert a spherically-shaped, collimated incident beam into a line-shaped beam with Gaussian intensity distribution along the major and minor axis of the beam as shown in (Fig.1). In contrast, Powell lenses utilize a two-dimensional aspheric, conically-shaped front surface, described with Eq. (1):

$$z(r) = \frac{cr^2}{1 + \sqrt{1 - (1 + k)(cr)^2}}$$

to generate a line-shaped beam with almost uniform intensity distribution along the line direction. Here **r** is the radius of the front surface's curvature, **k** is the conic parameter, and **c** is the curvature of a sphere. A Powell lens does not have a well-defined focal length and instead is characterized by a fan angle, which is defined as the maximum expansion angle of the beam in the line direction. The conical surface of the Powell lens introduces spherical aberrations in the propagating optical beam to generate an output beam with almost uniform intensity profile along the line direction, except for edge effects at the ends of the line as shown in Fig.1 (D-F). The back surface of the Powell lens can be either planar or curved, and its profile is used to control the fan angle.

2.2 Layout of PL-LS-SD-OCT system

A schematic diagram of the PL-LF-SD-OCT system is shown in Fig.2. The system is powered by a supercontinuum laser (SuperK Extreme, NKT Phonics) and a custom filter unit is used to select a portion of the emission spectrum suitable for this study. A reflective collimator (RC04APC-P01, Thorlabs) is used to generate a collimated beam with 3.9 mm $1/e^2$ diameter and output power of ~12 mW. A Powell lens with 5º fan angle is used to generate a line-shaped beam in the vertical (Y) direction. A telecentric pair of achromat doublets (L1 f = 75 mm and L2 f = 100 mm) is used to relay and magnify the beam. A non-polarizing beamsplitter (BS023, Thorlabs) is used to split the incident beam between the sample and the reference arms of the Michelson interferometer. Multiple slits are used throughout the system to eliminate unwanted reflections from the optical components.

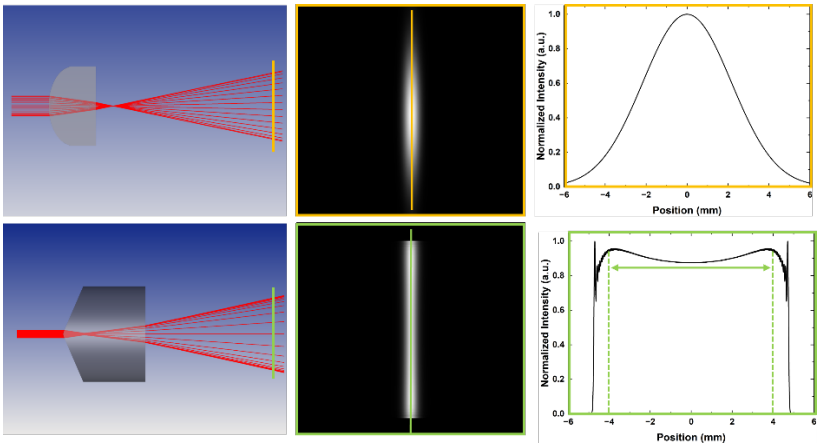

Fig. 1. Zemax simulations of beam propagation though a cylindrical lens (A) and a Powell lens (D). 1D and 2D cross-sectional light intensity distributions for the cylindrical (B and C) and Powell (E and F) lenses.

In the sample arm of the system, the beam is focused (in X direction) onto a 1D galvanometric scanner (GVS011, Thorlabs) to allow for acquisition of volumetric images.. A telecentric pair of achromat doublets (L3 = 80 mm and L4 = 100 mm) is used to relay and magnify the beam in order to partially fill (~60%) the entrance aperture of a microscope objective (M Plan APO NIR 10×/0.26NA, Mitutoyo). The optical power measured at the focal plane of the microscope objective is 2.5mW, which is below the maximum permissible exposure for human corneal and retinal tissue imaging as defined by the ANSI standard [19].

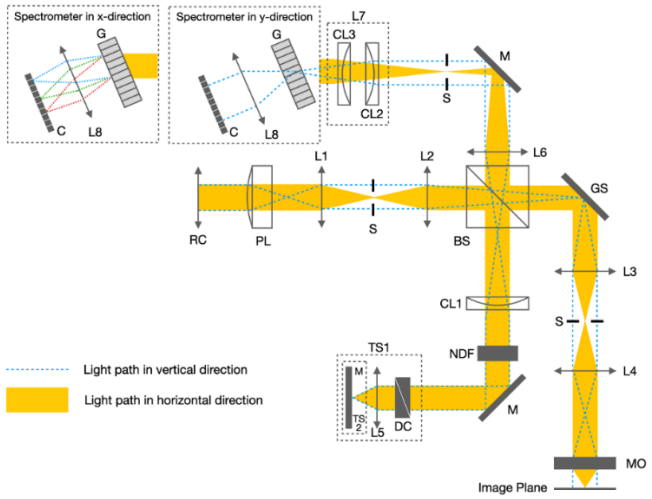

Fig. 2. A schematic diagram of the PL-LS-SD-OCT system. RC, reflective collimator; PL, Powell lens; L1-L6, achromatic doublets; BS, non-polarized beam splitter; CL, cylindrical lens; NDF, neutral density filter; TS, translation stage; DC, dispersion compensation unit; M, mirror; GS, galvanometric scanner; MO, microscopic objective; S, adjustable slit; G, transmissive grating; L8, camera lens; C, camera CMOS sensor. PL = 5° fan angle, L1 = 75mm, L2 = L4 = 100mm, L3 = 80mm, L5 = 30mm, L6 = 200mm, L8 = 85mm, CL1 = 75mm, CL2 = 150mm, and CL3 = 250mm.

In the reference arm of the system, a cylindrical lens, CL1 (f = 75 mm) forms a telecentric pair with L2 in the vertical direction to convert the line-shaped beam into a circular one. Neutral density filters (NDF) are mounted along the optical path after CL1 to prevent saturation of the camera. A custom-built dispersion compensation unit (a pair of BK7 prisms) is used to compensate low orders of dispersion mismatch introduced by the optical components of the sample and reference arms (what we refer to as "hardware dispersion compensation", or HDC). A custom Matlab (Mathworks) algorithm is used to compensate numerically higher orders of dispersion using a procedure similar to the one described in reference [20]. An achromat doublet L5 (f = 30 mm) is used to focus the reference beam onto a mirror, mounted on a small translation stage. The mirror, L5 and the DC unit are mounted onto a large linear translation stage to control the optical path difference between two arms.

In the detection arm of the system, a combination of lenses, L6 and L7 is used to relay the beam to the spectrometer. L6 is an achromat doublet (f = 200 mm), while L7 represents a pair of cylindrical lenses (CL2 and CL3) with mutually orthogonal orientation, that are used to control the magnification of the beam separately in the X and Y direction[21]. The spectrometer is comprised of a volume phase holographic (VPH) transmission grating (990 l/mm @ 805nm, Wasatch Photonics), and a camera lens (Planar T* 1.4/85, Zeiss). The transmitted optical beam is projected onto the sensor of a 2D CMOS camera (J-PRI, AOS technologies). The camera sensor has an area of 2,560 × 1,920 pixels, with a pixel size of 7.8 μm × 7.8 μm and maximum data acquisition rate of 2,000 fps. Higher frame rates can be achieved by selecting smaller active areas of the sensor. For this design of the PL-LF-SD-OCT system, all 2,560 pixels were utilized in the spectral direction in order to achieve largest possible OCT scanning range. In the spatial (B-scan) direction, only 600 pixels were used for volumetric image acquisition, resulting in maximum achievable data acquisition rate of 6,000 fps..

2.3. Data acquisition and processing

A custom Labview-based algorithm was developed for data acquisition with the PL-LS-SD-OCT system. A set of custom Python-based algorithms were developed for processing of the raw data and generation of dispersion compensated images. Amira (ThermoFisher Scientific) was used to render volumetric images and display enface projections from selected regions of interest.

3. Results

3.1. System performance

The performance of the PL-LS-SD-OCT system in terms of resolution and sensitivity was evaluated using either a protected silver mirror or a United States Air Force (USAF 1951) resolution target as the imaged object, and results from the tests are summarized in Fig, 3. The spectra measured separately at the detection arm of the system from mirror reflections in the reference and sample arms of the system are shown in Fig. 3A. Note that the spectra were generated by averaging 50 consecutive frames to suppress the effect from the random intensity noise (RIN) of the laser. The detected spectrum is centered 730 nm with a FWHM spectral bandwidth of 135 nm. Fig.3 (B) shows the system's axial point-spread function (PSF) measured at a depth of 100 μm relative to the zero-delay line after hardware dispersion compensation (HDC) only (black color) and after additional software dispersion compensation (SDC, red color). The PSF's FWHM is ~1.8 μm in free space, corresponding to ~1.3 μm in biological tissue assuming an averaged reflective index of 1.38. The system's axial resolution degrades slowly with depth, only by 6% over 1 mm scanning range (Fig. 3C). The system's sensitivity was measured for 2.5 mW incident optical power and 2,000 fps camera rate. As shown in Fig. 3D, the maximum sensitivity measured at a depth of ~100 μm is ~87 dB with ~ 6 dB sensitivity

roll-off over 700 µm and ~13 dB roll-off over the 1 mm scanning range (Fig, 3D). Figure 3E shows the sensitivity results for all 600 A-scans within a single B-scan, measured at a depth location of 100 µm away from the zero-delay line. These results show only ~1.6 dB loss of sensitivity from the center of the B-scan to its edges.

The system's lateral resolution was evaluated by imaging a USAF 1951 resolution target. With the current design of the system, the FOV is 263 µm (X) × 658 µm (Y), corresponding to 300 B-scans (X) and 600 A-scans in each B-scan (Y). Figure 3F shows an image of groups 6 and 7 of the resolution target. The intensity plots shown in Fig. 3G correspond to the locations in Fig. 3F marked with the green and red lines. Since both the horizontal and vertical bars of group 7, element 6 can be clearly resolved and the width of 1 line pair of this element is equivalent to 2.2 µm, therefore both the horizontal and vertical transverse resolution of the PL-LF-SD-OCT system are better than 2.2 µm.

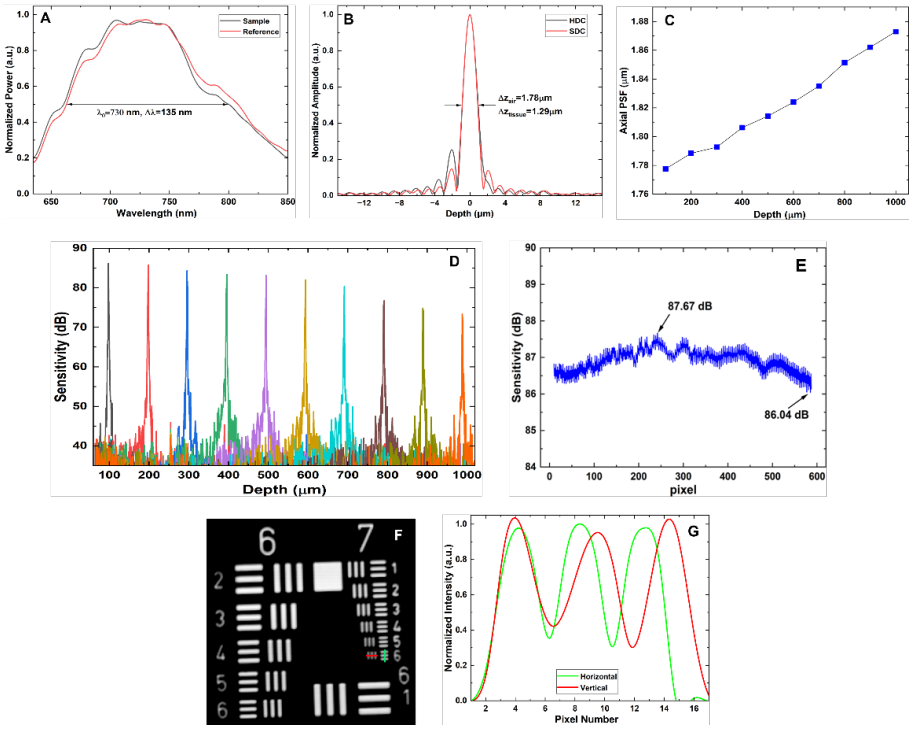

Fig. 3. Spectra from the reference and sample arms measured at the detection end of the system (A). Axial PSF measured at depth of 100 µm after HDC and HDC + SDC (B). Depth-dependent degradation of the axial resolution (C). Depth-dependent sensitivity (D). Sensitivity distribution along the B-scan, measured at 100 µm depth (E). Image of the USAF 1951 resolution target (F). Intensity profiles acquired from Group 7, Element 6 at the locations marked with the green and red lines in Fig. 3F (G).

3.2 Images of biological tissue

While the PL-LF-SD-OCT system is designed for imaging the human anterior eye segment (cornea and limbus), due to COVID-19 related restrictions on conducting clinical imaging studies, ethics clearance for use of the PL-LF-SD-OCT system for *in-vivo* imaging of the human anterior segment (cornea and limbus) has been delayed. Therefore, the performance of the

system was evaluated by imaging plant tissue such as cucumber that has optical properties and cellular structure with size of the smallest cells similar to that of the human cornea, as well as imaging animal corneas (rats). For all imaging sessions, the optical power incident on the surface of the imaged object was 2.5 mW and the camera acquisition rate was set to 2,000 fps.

3.2.1. Cucumber

Fig. 4 (A) shows a digital photograph of a transverse slice from cucumber. A magnified view (6×) of the region of interest marked with the red square in Fig. 4A is shown in Fig. 4B. The red arrow marks a cucumber seed with semi-transparent surrounding tissue. Figures 4 (C-H) were generated using Amira software. XZ, YZ and enface (XY) images of the cucumber seed and the surrounding tissue are shown in Fig. 4C, 4D and 4E respectively, while Fig. 4F shows a volumetric image of the same region. Figures 3H and 3G show two enface images from the same 3D stack that correspond to different depths. Small cells of ~10 µm in size (Fig. 3G, red arrow) located along the boundary of the cucumber seed (white arrow), as well as cellular nuclei in the larger cells are clearly resolved. Small reflective features were observed in the cytoplasm of larger cells (Fig. 3H, green arrow), as well as double nuclei in one of the larger cells (Fig. 3H, blue arrow).

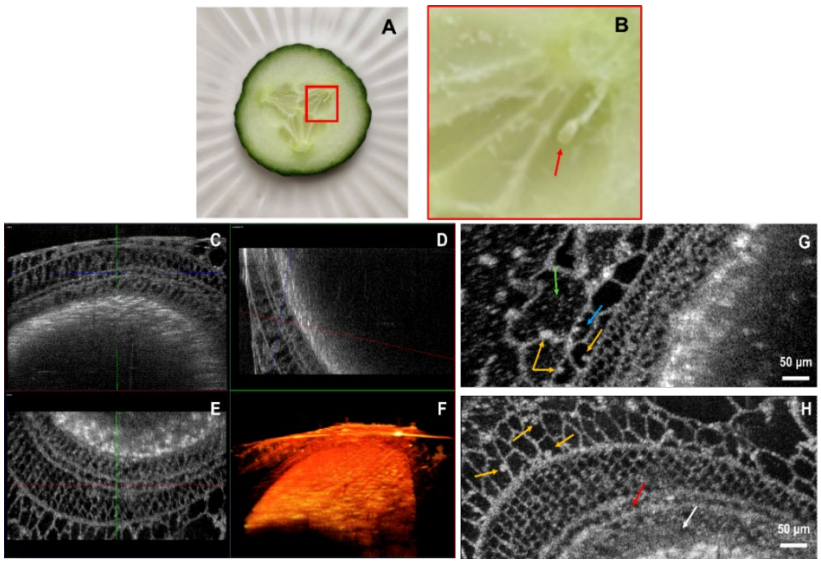

Fig. 4. Images of cucumber tissue. Digital photograph of transverse slide from cucumber (A). magnified view of the region of interest marked with the red square (B). PL-LS-SD-OCT images of the cucumber: XZ projection (C), YZ projection (D), enface projection (E), volumetric image (F), two enface projections corresponding to different depths (H and G). Cellular features are marked with colored arrows in figures 4H and 4G: seed (white), small cells (red), cellular nuclei (orange), reflective features in the cytoplasm (green), cell with 2 nuclei (blue).

3.2.2. Rat cornea

The corneas of male Sprague-Dawley rats (~ 1 year old) were imaged with the PL-LF-SD-OCT system. All imaging sessions were conducted in compliance with the ethics regulations of the Office of Research Ethics, University of Waterloo. Immediately after euthanasia, rats were placed on a holder mounted on a XYZ translations stage as shown in the digital photograph in Fig. 5A. A representative B-scan (XZ direction) of the rat cornea is shown in Fig. 5B.

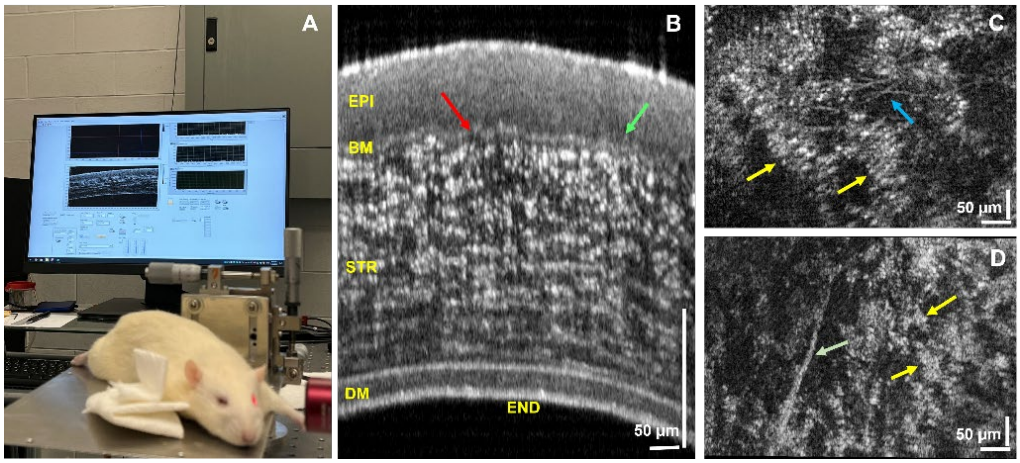

Fig.5. Digital photograph of the imaged animal (A). Representative B-scan of the rat cornea (B)EPI -Epithelium; BM – Bowman's membrane; STR - Stroma; DM - Descemet's membrane; END - Endothelium; Red arrow: Bowman's layer, green arrow – basal cell layer of the epithelium. Enface projections acquired from the anterior (C) and posterior (D) stroma. Arrows mark: keratocytes (yellow); thin nerves in the anterior stroma (blue); thick nerve in the posterior stroma (white).

While all 5 of the major corneal layers (EPI – epithelium; BM – Bowman's membrane; STR – stroma; DM - Descemet's membrane; and END – endothelium) are clearly resolved in the image, many of these layers appear blurred. The blur is caused by the very short (~18 µm) depth-of-focus of the current design of the PL-LF-SD-OCT system. For the imaging data presented in Fig. 5 (B-D), the focal plane of the microscope objective was positioned at the anterior stroma to allow for imaging of keratocyte cells. The red arrow in Fig 5B marks the Bowman's membrane, while the green arrow marks the basal cell layer in the corneal epithelium. Figures 5C and 5D show enface projections acquired from different locations the anterior and posterior stroma respectively. The yellow arrows mark stromal keratocytes, the blue arrow – thin corneal nerves in the anterior stroma, white arrow – larger stomal nerve located in the posterior stroma.

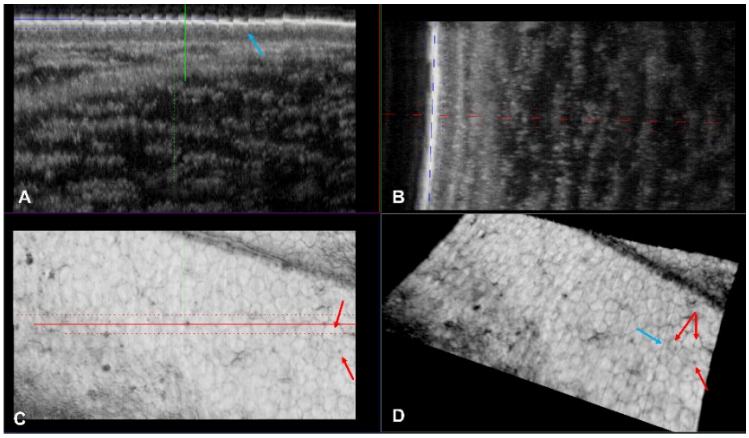

Fig.6. Images of the corneal endothelium. XZ (A) and YZ (B) cross-sectional images of the posterior cornea showing the Descemet's membrane and the endothelium. Enface images of the endothelium (C and D) showing the cellular structure. Red arrows mark cellular nuclei, blue arrows mark artefacts generated by the integer-based flattening algorithm.

Cross-sectional and enface images of the posterior rat cornea that were acquired with the focal plane positioned at the endothelial layer are shown in Figure 6. The cross-sectional images (Fig. 6A and 6B) were flattened and enface images of the endothelial layer (Fig. 6C and 6D) were generated using maximum intensity projection (MIP) projection. The enface images (Fig. 6C and 6D) clearly show the honeycomb-like pattern of the endothelial cells, as well as dark, round spots inside the cells that correspond to cellular nuclei (red arrows). Line artefacts in the enface images (Fig. 6D, blue arrow) are caused by the integer septs in the flattening algorithm.

4. Discussion

The novel design of the PL-LF-SD-OCT system resulted in very high spatial resolution in biological tissue: ~2 µm isotropic lateral and ~ 1.3 µm axial (Fig. 3B, 3G and 3F), which was sufficient to visualize the cellular and sub-cellular structure of plant tissues (Fig. 4) and animal cornea (Fig. 5 and Fig. 6). Furthermore, the broadening of the axial PSF function over the entire scanning range (1 mm) was limited to only ~ 6% (Fig. 3C) compared to nearly 100% change reported by the Singaporean research group[18] over a scanning range of ~ 850 µm. Maximum sensitivity of 87 dB was achieved (Fig, 3D) for 2,000 fps image acquisition rate and 2.5 mW imaging power, which is well below the MPE recommended by the ANSI standard for *in-vivo* imaging of human ocular tissue. Given equal conditions (same frame rate and imaging power), the novel design proposed here offers an improvement of ~ 5 dB in the maximum sensitivity measured close to the zero delay line, compared to the design proposed by the Singaporean group[18]. A very important feature of the proposed novel design is the small (only ~ 1.6 dB) loss of sensitivity along the width of a B-scan (Fig. 3E), which is a very significant improvement compared to the sensitivity loss associated with LF-OCT systems based on cylindrical line generators (~10 dB or higher)[5-10, 12-15]. Since the Singaporean research group[18] has not reported the B-scan sensitivity loss for their design, unfortunately, we cannot provide direct comparison between the 2 designs at this time.

While the current design of the novel PL-LF-SD-OCT system offers sufficiently high spatial resolution and sensitivity for imaging the cellular structure of semi-transparent biological tissues such as cucumber (Fig. 4) and rat cornea (Fig. 5 and Fig. 6), the design leaves plenty of room for improvement:

a) **Depth of focus (DOF):** The current design resulted in ~18 µm DOF, which is too short for imaging the cellular structure of the human cornea in one volumetric data set, as seen in Fig 5B. One approach to resolving this issue would be to trade lateral resolution for extended DOF by replacing the microscope objective in the current design with a lower magnification one. However, this approach is not desirable, as it will compromise the ability to visualize the cellular structure of corneal tissue, which was the main goal for designing the new PL-LF-SD-OCT system. An alternative approach would be to apply digital adaptive optics (DAO)[7, 25-28] to correct for defocus and higher order aberrations in the PL-LF-SD-OCT images. We plan to utilize this approach in the near future.

b) **Sensitivity and sensitivity roll-off:** The current design offers maximum sensitivity of 87 dB near the zero-delay line with ~13 dB sensitivity roll-off (Fig. 3D), which is sufficient for imaging the cellular structure of semi-transparent tissues such as the human and animal cornea, though will be problematic for imaging biological tissues that are more scattering such as skin. The sensitivity of the novel PL-LF-SD-OCT system is dependent on several factors: imaging power, image acquisition rate and efficiency of the optical design. Increasing safely the imaging power so that it is below the ANSI recommended MPE for ocular tissues is a very limited option, and in our case can result in only ~1.5 dB sensitivity gain. Decreasing the camera acquisition rate to 1,000 fps will result in 3 dB sensitivity gain, however, this approach will introduce unwanted unvoluntary eye motion artefacts in the *in-vivo* human corneal images[8, 29]. The current optical design of the sample and detection arms of the PL-LF-SD-OCT system include a large number of optical components that are lossy. Optimizing the efficiency of the

collection of light scattered from the imaged object should improve the system's sensitivity. Furthermore, the camera pixel size is small (7.8 μm × 7.8 μm), which poses significant constraints on the optical design of the spectrometer and the PL-LF-SD-OCT system as a whole. The use of a camera with larger pixel size would improve the system's sensitivity, as well as the sensitivity roll-off, however, this approach will result in shorter scanning range for the same spectral range. Camera efficiency is another factor that contributes to the system's sensitivity. The use of cameras with better quantum efficiency would improve the system's sensitivity and possibly the sensitivity roll-off.

c) **Powell lens:** While the use of a Powell lens greatly reduced the loss of sensitivity along the width of a B-scan compared to cylindrical lens-based LF-OCT systems, integration of the Powell lens in an OCT system is challenging. As the Powell lens does not have a very well-defined focus, it is difficult to generate a collimated beam in the reference arm of the OCT system to allow for changes in the reference pathlength without significant loss of system's sensitivity due to misalignment between the refence and sample arm beams. In our case, this issue was resolved by use of a cylindrical lens in the reference arm to convert the line-shaped beam to approximately circular and collimated beam in the refence arm of the system. Also, it should be noted that the quality of the Powell lens varies between manufacturers and imprecision in the Powell lens design can affect negatively both the resolution and the sensitivity of the PL-LF-SD-OCT system.

While only images of rodent cornea acquired post mortem were presented in this paper (Fig. 5 and Fig. 6), future biomedical applications of the novel PL-LF-SD-OCT system will focus on *in-vivo* imaging studies of the healthy and pathological human cornea and limbus. The design of the system can be adapted for retinal imaging by re-designing the sample arm of the PL-LF-SD-OCT system. By increasing the imaging power and decreasing the image acquisition rate, the current design of the system may also be suitable for imaging skin and other highly scattering biological tissues for different biomedical applications.

5. Conclusions

A novel PL-LF-SD-OCT system that utilizes a Powell lens instead of cylindrical lens as the line generator was developed. This design resulted in significantly improved uniformity of the illumination along the line direction and only ~ 1.6 dB sensitivity loss between the B-scan's center and edges. The system's high spatial resolution allowed for imaging the cellular structure of plant tissues and the animal cornea, as well as resolving small morphological features such as cellular nuclei in the endothelial cells. Future clinical applications of the PL-LS-SD-OCT system include *in-vivo* imaging of the healthy and pathological human cornea and limbus.

Funding. Canadian Institutes of Health Research (PJT-178018); Natural Sciences and Engineering Research Council of Canada (RGPIN-2020-06308 and RTI-2021-00780).

Acknowledgments. The authors would like to thank Jean Flanagan for assistance with the animal imaging.

Disclosures. The authors declare no conflicts of interest related to this article.

Data availability. Data underlying the results presented this paper are not publicly available at this time but may be obtained from the authors upon reasonable request.

References

1. W. Drexler and J. G. Fujimoto, eds., *Optical Coherence Tomography*, 2nd ed. (Springer Cham, 2015).
2. E. Beaurepaire, A. C. Boccara,M. Lebec, L. Blanchot, and H. Saint-Jalmes, "Full-field optical coherence microscopy," Opt. Lett. 23, 244–246 (1998).
3. B. Grajciar, M. Pircher, A. Fercher, and R. Leitgeb, "Parallel Fourier domain optical coherence tomography for *in vivo* measurement of the human eye," Opt. Express 13, 1131–1137 (2005).
4. B. Grajciar, Y. Lehareinger, A. Fercher, and R. Leitgeb, "High sensitivity phase mapping with parallel Fourier domain optical coherence tomography at 512 000 A-scan/s," Opt. Express 18, 21841–21850 (2010).

5. A. F. Zuluaga and R. Richards-Kortum, "Spatially resolved spectral interferometry for determination of subsurface structure," Opt. Lett. 24, 519–521 (1999).
6. D. J. Fechtig, B. Grajciar, T. Schmoll, C. Blatter, R. M. Werkmeister, W. Drexler, and R. A. Leitgeb, "Line-field parallel swept source MHz OCT for structural and functional retinal imaging," Biomed. Opt. Express 6, 716–735 (2015).
7. L. Ginner, A. Kumar, D. Fechtig, L. M. Wurster, M. Salas, M. Pircher, and R. A. Leitgeb, "Noniterative digital aberration correction for cellular resolution retinal optical coherence tomography *in vivo*," Optica 4, 924–(2017).
8. L. Ginner, T. Schmoll, A. Kumar, M. Salas, N. Pricoupenko, L. M. Wurster, and R. A. Leitgeb, "Holographic line field enface OCT with digital adaptive optics in the retina *in vivo*," Biomed. Opt. Express 9, 472–485 (2018).
9. V. P. Pandiyan, X. Jiang, A. Maloney-Bertelli, J. A. Kuchenbecker, U. Sharma, and R. Sabesan, "High-speed adaptive optics line-scan OCT for cellular-resolution optoretinography," Biomed. Opt. Express 11, 5274–5296 (2020).
10. V. P. Pandiyan, X. Jiang, J. A. Kuchenbecker, and R. Sabesan, "Reflective mirror-based line-scan adaptive optics OCT for imaging retinal structure and function," Biomed. Opt. Express 12, 5865–5880 (2021).
11. V. P. Pandiyan, A. Maloney-Bertelli, J. A. Kuchenbecker, K. C. Boyle, T. Ling, Z. C. Chen, B. H. Park, A. Roorda, D. Palanker, and R. Sabesan, "The optoretinogram reveals the primary steps of phototransduction in the living human eye," Sci. Adv. 6, eabc1124 (2020).
12. L. Han, B. Tan, Z. Hosseinaee, L. K. Chen, D. Hileeto, and K. Bizheva, "Line-scanning SD-OCT for *in-vivo*, non-contact, volumetric, cellular resolution imaging of the human cornea and limbus," Biomed. Opt. Express 13, 4007–4020 (2022).
13. A. Davis, O. Levecq, H. Azimani, D. Siret, and A. Dubois, "Simultaneous dual-band line-field confocal optical coherence tomography: application to skin imaging," Biomed. Opt. Express 10, 694–706 (2019).
14. A. Dubois, O. Levecq, H. Azimani, A. Davis, J. Ogien, D. Siret, and A. Barut, "Line-field confocal time-domain optical coherence tomography with dynamic focusing," Opt. Express 26, 33534–33542 (2018).
15. A. Dubois, W. Xue, O. Levecq, P. Bulkin, A.-L. Coutrot, and J. Ogien, "Mirau-based line-field confocal optical coherence tomography," Opt. Express 28, 7918–7927 (2020).
16. E. Cinotti, M. Bertello, A. Cartocci, D. Fiorani, L. Tognetti, V. Solmi, S. Cappilli, K. Peris, J. L. Perrot, M. Suppa, V. Del Marmol, and P. Rubegni, "Comparison of reflectance confocal microscopy and line-field optical coherence tomography for the identification of keratinocyte skin tumours," Ski. Res. Technol. 29, e13215 (2023).
17. I. Powell, "Design of a laser beam line expander," Appl. Opt. 26, 3705–3709 (1987).
18. Z. Al-Qazwini, Z. Y. G. Ko, K. Mehta, and N. Chen, "Ultrahigh-speed line-scan SD-OCT for four-dimensional *in vivo* imaging of small animal models," Biomed. Opt. Express 9, 1216–1228 (2018).
19. ANSI Z80.36-2016, Ophthalmics, Light Hazard Protection for Ophthalmic Instruments.
20. S. Saghafi, K. Becker, C. Hahn, and H.-U. Dodt, "3D-ultramicroscopy utilizing aspheric optics," J. Biophotonics 7, 117–125 (2013).
21. B. Cense, N. A. Nassif, T. C. Chen, M. C. Pierce, S.-H. Yun, B. H. Park, B. E. Bouma, G. J. Tearney, and J. F. de Boer, "Ultrahigh-resolution high-speed retinal imaging using spectral-domain optical coherence tomography," Opt. Express 12, 2435–2447 (2004).
22. S. Chen, X. Liu, N. 327 Wang, X. Wang, Q. Xiong, E. Bo, X. Yu, S. Chen, and L. Liu, "Visualizing micro-anatomical structures of the posterior cornea with micro-optical coherence tomography," Sci. Reports 7 (2017).
23. Y.-T. Chen, C.-Y. Tsai, Y.-K. Chiu, T.-W. Hsu, L.W. Chen,W.-L. Chen, and S.-L. Huang, "En face and cross-sectional corneal tomograms using sub-micron spatial resolution optical coherence tomography," Sci. Reports 8 (2018).
24. M. Ang, A. Konstantopoulos, G. Goh, H. M. Htoon, X. Seah, N. C. Lwin, X. Liu, S. Chen, L. Liu, J. S. Mehta, and et al., "Evaluation of a micro-optical coherence tomography for the corneal endothelium in an animal model," Sci. Reports 6 (2016).
25. S. G. Adie, B. W. Graf, A. Ahmad, P. S. Carney, and S. A. Boppart, "Computational adaptive optics for broadband optical interferometric tomography of biological tissue," Proc. National Acad. Sci. 109, 7175–7180 (2012).
26. A. Kumar, W. Drexler, and R. A. Leitgeb, "Numerical focusing methods for Full Field OCT: a comparison based on a common signal model," Opt. Express 22, 16061–16078 (2014).
27. D. Borycki, E. Auksorius, P. Węgrzyn, and M. Wojtkowski, "Computational aberration correction in spatiotemporal optical coherence (STOC) imaging," Opt. Lett. 45, 1293–1296 (2020).
28. A. Kumar, T. Kamali, R. Platzer, A. Unterhuber, W. Drexler, and R. A. Leitgeb, "Anisotropic aberration correction using region of interest based digital adaptive optics in Fourier Domain OCT," Biomed. Opt. Express 6, 1124–1134 (2015).
29. M. F. Kraus, B. Potsaid, M. A. Mayer, R. Bock, B. Baumann, J. J. Liu, J. Hornegger, and J. G. Fujimoto, "Motion correction in optical coherence tomography volumes on a per a-scan basis using orthogonal scan patterns," Biomed. Opt. Express 3, 1182–1199 (2012).